RESEARCH ARTICLE

Key Points:
- The heat advection driven by the barotropic geostrophic current is the dominant component in the total heat advection
- The energy of the heat advection is redistributed within different time scales due to the cross-spectral interaction
- About 47% of the energy in the heat advection retained within the original band

Correspondence to:
X.-H. Yan,
xiaohai@udel.edu

The horizontal heat advection in the Middle Atlantic Bight and the cross-spectral interactions within the heat advection

Jin Sha[1,2] , Xiao-Hai Yan[2,3] , and Xiaoming Li[1,4]

[1]Digital Earth Laboratory, Institute of Remote Sensing and Digital Earth, Chinese Academy of Sciences, Beijing, China, [2]College of Earth, Ocean, and Environment, University of Delaware, Newark, Delaware, USA, [3]University of Delaware/Xiamen University Joint Institute of Coastal Research and Management, Newark, Delaware, USA, [4]Hainan Key Laboratory of Earth Observation, Sanya, China

Abstract The upper ocean horizontal heat advection over the middle and outer shelf of the Middle Atlantic Bight (MAB) is investigated using satellite and in situ observations. In the upper mixed layer, the heat advection is mostly positive indicating that it decreases the shelf heat content by bringing cold water from upstream. The domain-averaged heat advection driven by the barotropic geostrophic current is one-order larger relative to the density-driven geostrophic shear and the wind-driven current. The barotropic geostrophic advection components in the alongshore and offshore direction are of the same order. To investigate the temporal properties of the heat advection, the temperature and currents are decomposed into different time scales using Fast Multidimensional Ensemble Empirical Decomposition (FMEEMD). The cross-spectral interactions within the advection are quantitatively evaluated with major components identified. Due to the cross-spectral interaction, energy within the heat advection is found to be redistributed through different time scales, with at least 46.5% variation retained within the original band for the barotropic geostrophic advection. Our results help to better understand the temporal variability of the heat advection, provide a baseline of the nonlinear energy transfer framework within different time scales in the heat advection, and imply the possibility of interplays between short and long-term oceanic phenomena.

1. Introduction

Variations of the ocean heat content are gaining increased attention in the context of the global climate change [*Levitus et al.*, 2012; *Chen and Tung*, 2014]. Studies suggested that the roles of the surface heat flux and ocean heat transport, which directly relate to the heat content, may vary on different time scales [*Kushnir*, 1994; *He and Weisberg*, 2002, 2003; *Gulev et al.*, 2013] and are subjected to regional differences [*Halliwell*, 1998; *Dong and Kelly*, 2004]. In the Middle Atlantic Bight (MAB), the sea surface heat flux is balanced by the heat advection especially the along-isobath heat advection in the sense of the long-term mean [*Lentz*, 2009]. On time scales from days to weeks, the heat advection drives the temperature variability over the New England shelf [*Lentz et al.*, 2010]. On the seasonal scale, the ocean heat content is dominated by the surface net heat flux [*Mountain et al.*, 1996; *Beardsley et al.*, 2003; *Lentz et al.*, 2010]. Concerning the interannual variability of the temperature, a study over the Long Island Sound reveals that it is the horizontal heat advection dominating the temperature variability [*Lee and Lwiza*, 2005]. Also the interannual variability of the wintertime cooling of the inner shelf is partially influenced by the alongshore heat advection [*Connolly and Lentz*, 2014]. *Shearman and Lentz* [2009] show that the long-term temperature variability along the U.S. east coast is controlled by the along shelf transport. The study of *Grodsky et al.* [2017] also suggests the importance of the horizontal advection to the temperature interannual oscillations.

Despite the importance and varying roles of the heat advection in the heat budget over MAB, it is not yet fully clarified how the heat advection varies spatially and temporally. Satellite remote sensing gives us a chance to investigate the horizontal heat advection over the shelf synoptically. Also, provided by more than 20 years' continuous observation, it is possible to decompose the temperature and currents into components of different time scales, which could help to quantitatively analyze the temporal variation of the horizontal heat advection. This would be essential to further understand the response of the ocean to the climate change.
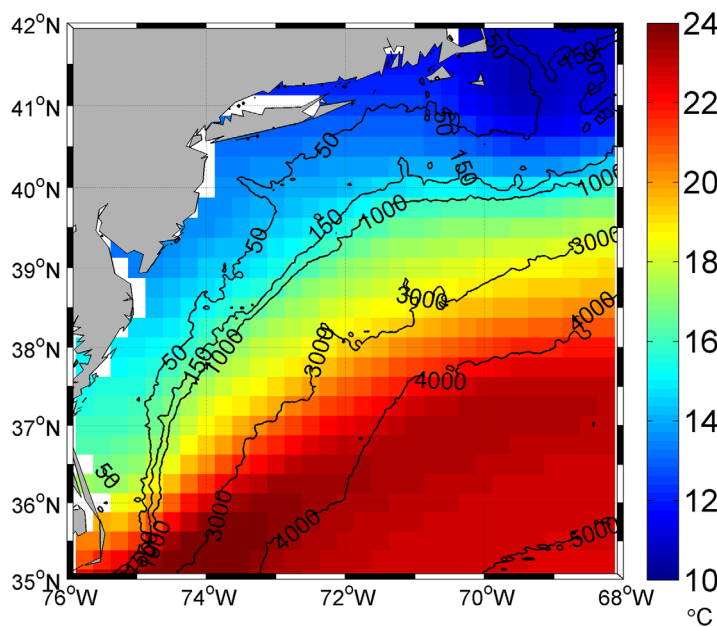
In this study, the horizontal heat advection within the mixed layer depth is investigated by considering three major current components driven by the sea level pressure, by the density gradient, and by the wind. The data sets and the methods used are described in section 2. The comparison of advection components of different driven forces and of different directions (alongshore and offshore) are shown in section 3. The heat advection components at different time scales are quantitatively estimated and analyzed in the frequency domain in section 4. Finally, we discuss the energy exchange among different time scales in section 5.

2. Data and Methods

2.1. Data

The sea surface temperature (SST) data set used in this study is the Optimum Interpolation Sea Surface Temperature (OISST ver.2, AVHRR-only) from 1981 to 2014, with the spatial resolution of 0.25° and the temporal resolution of 1 day (Figure 1). The total error (standard deviation), which is derived from the random, sampling and bias error, for the AVHRR-only product is approximately 0.4°C–0.6°C close to the east coast of United States comparing to the in situ measurements from ships and buoys [*Reynolds et al.*, 2007].

To derive the surface absolute geostrophic velocities, we used the Maps of Absolute Dynamic Topography (MADT), which is released by AVISO/CNES containing daily maps from 1993 to 2016 on a 0.25° Cartesian grid with tidal and inverse barometer corrections. The product is the DUACS 2014 version firstly released in 2014 which uses a reference period of 20 years. MADT is the sum of sea level anomaly (SLA) and mean dynamic topography (MDT). The MDT refers to the Mean Sea Surface Height minus Geoid, by combining GRACE, altimeter, and in situ measurements [*Rio et al.*, 2011]. The time-varying sea level is generally considered with an error of 2∼3 cm [*Cheney*, 1994], yielding geostrophic velocity errors of 12–18 cm/s over the distance of 25 km. *Rio et al.* [2011] made a detailed evaluation of the MDT and MADT. They found that the MDT shows a consistent pattern over the continental shelves comparing with in situ measurements and the geostrophic velocities from MADT have errors in the order of 12 cm/s over the broad Gulf Stream Current Area (20°N–60°N, 275°E–340°E) [*Rio et al.*, 2011]. Despite the uncertainty of the SLA over the shallow waters, this data set is valuable to describe physical processes on the continental shelf [e.g., *Ruiz et al.*, 2009; *Gawarkiewicz et al.*, 2012; *Strub et al.*, 2015; *Ruiz Etcheverry et al.*, 2016]. Moreover, if taken monthly mean, the error of the derived velocities will be further reduced (e.g., 4∼6 cm/s given a SLA decorrelation scale of 4 days) [*Ponte*, 1994]. In this study, due to the energetic tidal mixing and the land contamination, the inner shelf areas within 25 km offshore are excluded, and monthly averaged data are used and therefore time scales less than 2 months are not considered here.

To quantify the contribution of the Ekman transport, we use the blended sea winds [*Zhang et al.*, 2006] from National Climatic Data Center (NCDC) of NOAA. The data set contains monthly ocean surface winds and wind stresses on a global 0.25° grid from 1987 to 2011. The product has a zonal speed bias of 0.12 m/s and a meridional speed bias of 0.055 m/s, with root-mean-square error being less than 2 m/s within the Atlantic Ocean for both directions comparing with in situ buoy measurements [*Peng et al.*, 2013].

Monthly climatological temperature and salinity profiles come from the World Ocean Atlas 2013 version 2 (an updated version of WOA13) [*Locarnini et al.*, 2013], as 0.25°-gridded monthly

Figure 1. The mean OISST data set (1983–2014) over the Middle Atlantic Bight and ambient open oceans. The black lines are the bathymetry.

data sets (12 month, averaged over decades) at WOA standard depth level (e.g., 5 m for the first 100 m depth). The temperature profiles are used to determine the mixed layer depth (MLD) as stated in section 2.2. The density profiles derived from the temperature and salinity are used to determine the horizontal density gradient as used in section 2.3. Moreover, the gridded subsurface temperature maps from Simple Ocean Data Assimilation (SODA v2.2.4) [*Carton et al.*, 2005] between 1990 and 2010 are also employed as a complementary data set to determine the mixed layer depth. The SODA is a monthly data set on a 0.125° × 0.25° × 40 grid incorporating WOA and satellite SST measurements.

All above data sets are subject to different temporal coverage and spatial grids. Hence first of all these products are projected into a common grid of 1/8° with 1 m vertical resolution and a monthly common period (1993–2014) using the linear interpolation. We use a finer grid of 1/8° to keep the data coverage to a better extent concerning values near the data margin may be lost in data processing steps such as the data collocating and gradient calculations. The study area is chosen between the 25 km offshore and the 1000 m isobaths (though the whole area from coast to 3000 m isobath is shown in our figures). Constrained by the data resolution and coverage, coastal and small-scale processes could not be resolved, thus only mesoscale flows over the shelf are investigated in this study.

2.2. Estimation of the Mixed Layer Depth
In our study, the upper ocean heat content is calculated by integrating from the surface to the mixed layer depth (MLD), which is determined from WOA monthly gridded temperature. By adopting such MLD, continuous SST observations for more than 20 years can be used as the approximation of the mixed layer temperature (MLT). *Grodsky et al.* [2008] made a comparison between the bulk sea surface and mixed layer temperatures, showing that globally and time-averaged MLT is cooler than SST by approximately 0.1°C with extreme values of 0.8°C at eastern equatorial Pacific. Since this study focuses on the heat advection, the temperature-based MLD definition is preferred than other methods [*de Boyer Montégut et al.*, 2007]. The threshold used to define the MLD is $\Delta T = 0.5°C$ from the surface water temperature. The MLD is first determined from the monthly temperature climatology, and then interpolated linearly over our common study period. The uncertainties of using such MLD are further discussed in the Appendix A.

2.3. Estimation of the Shelf Currents
The ocean currents contain components driven by different forces [*Dong and Kelly*, 2004; *Han et al.*, 2010]. In this study, we mainly consider three components: the barotropic geostrophic current due to the sloping sea surface ($\vec{u}_{elev}$), the geostrophic current shear due to the density gradient ($\vec{u}_{shear}$), and the Ekman transport due to the surface wind stress ($\vec{u}_{wind}$).Using the sea surface as the reference level [*Han et al.*, 2010], the total geostrophic current at depth z is given by

$$\vec{u}_g(x,y,z,t)$$
$$= \frac{g}{f}\vec{k}\times\nabla\eta(x,y,t) + \frac{g}{\rho_0 f}\int_{-z}^{0}\nabla\rho(x,y,z,t)\times\vec{k}\,dz \tag{1}$$
$$= \vec{u}_{elev} + \vec{u}_{shear}$$

where η is the sea surface elevation from the altimetry data, $g = 9.8\,\text{m/s}^2$, $f = 9.35\times10^{-5}\,\text{s}^{-1}$, $\vec{k}$ is the unit vector in the z direction (positive upward), and reference density $\rho_0 = 1025\,\text{kg/m}^3$. The density field is adopted from the WOA gridded monthly climatology.

For the wind-induced Ekman current, the depth-averaged wind current within the Ekman layer can be approximated as

$$\vec{u}_{wind} = \frac{1}{\rho_0 f D_E(x,y,t)}\left(\tau_y(x,y,t),\quad -\tau_x(x,y,t)\right), \tag{2}$$

with the Ekman depth D_E estimated as [*Garratt*, 1994; *Cushman-Roisin and Beckers*, 2011]

$$D_E = 0.4\frac{1}{f}\sqrt{\frac{|\vec{\tau}|}{\rho}}. \tag{3}$$

It should be noted that the Ekman transport can penetrate below the mixed layer. In such condition, the Ekman layer consists of the surface mixed layer and a transition layer where there is a velocity shear and

25∼50% Ekman transport occurs [*Lentz*, 1992]. For those cases, which takes about 6.7% of our total records, only Ekman currents occurred within the MLD are accounted for in the calculation.

2.4. Fast Multidimensional Ensemble Empirical Mode Decomposition (FMEEMD)

FMEEMD is used in this study to decompose the SST and MADT time series into oscillations on different time scales. The original Empirical Mode Decomposition (EMD) is a useful tool for the nonlinear, nonstationary time series, separating the data set into a finite number of intrinsic mode functions (IMFs) [*Huang et al.*, 1998]. That method identifies different oscillation cycles based on their characteristic temporal scales. The number of IMFs is determined by the length of the data set. To eliminate the mode-mixing phenomenon in the original EMD, an improved approach Ensemble Empirical Mode Decomposition (EEMD) [*Wu and Huang*, 2009] is proposed by adding white noise into the data and treating the mean of a sufficient number of trials as the final result. EEMD has been applied to decompose observations and extract the seasonal components [*Sha et al.*, 2015]. Afterward, Multidimensional EEMD (MEEMD) [*Wu et al.*, 2009] and Complementary EEMD (CEEMD) [*Yeh et al.*, 2010] are developed, respectively.

One most recent improvement is the Fast Multidimensional Ensemble Empirical Mode Decomposition (FMEEMD) [*Feng et al.*, 2014]. Using principal component analysis (PCA), the multidimensional climate data can be decomposed into principal component (PCs) and the corresponding empirical orthogonal functions (EOFs). Then the MEEMD is applied only to a small fraction of PCs so as to address the time consuming and data compression problems when processing gridded climate data. This method is validated by analyzing the extended reconstructed sea surface temperature (ERSST).

2.5. Decomposition of the Horizontal Heat Advection

The horizontal heat advection consists of three components depending on the driven forces considered in this study: the barotropic advection due to the sea surface elevation (the elevation advection hereafter), the baroclinic advection due to the density gradient (the shear advection), and the wind induced advection (the Ekman advection). In addition, these advections can be further decomposed in the alongshore direction and offshore direction, based on the smoothed bathymetry gradient.

The temporal variations of the heat advection are also investigated by decomposing both the current and the temperature into sets of oscillations on different time scales using FMEEMD:

$$Heat\ Advection = \vec{u} \cdot \nabla T = \sum_{i=1}^{5} \sum_{j=1}^{5} (\vec{u}_i \cdot \nabla T_j) \tag{4}$$

where i and j indicate the subseasonal (1–6 cycle/yr), seasonal (1 cycle/yr), interannual (0.1–1 cycle/yr), long-term and the mean modes, respectively. The subseasonal currents may relate to the mesoscale eddies or Rossby waves (with period of 90–120 days), while the long-term current variability may be associated with the large-scale sea level pressure patterns such as NAO (North Atlantic Oscillation) or AO (Arctic Oscillation). Those modes below the 95% significance level in FMEEMD are excluded. High-frequency oscillations with period less than 2 months could not be resolved by the monthly data. Limited by the time span of the records we are unable to recognize multidecadal oscillations with period longer than 10 years. Thus the long-term mode here refers to the residual by subtracting the subseasonal, seasonal, interannual, and mean modes from the original data.

The contribution of the advection temporal components ($\vec{u}_i \cdot \nabla T_j$), except the constant one with the mean velocity and the mean temperature ($\bar{\vec{u}} \cdot \nabla \bar{T}$), can be quantified using a contribution factor C_{ij}:

$$C_{ij} = \frac{std(\vec{u}_i \cdot \nabla T_j)}{\sqrt{\sum_{i=1}^{5} \sum_{j=1}^{5} std^2(\vec{u}_i \cdot \nabla T_j)}} \tag{5}$$

$$\sum_{i=1}^{5} \sum_{j=1}^{5} C_{ij}^2 = 1 \tag{6}$$

where *std* is the standard deviation of each mode in the temporal decomposition.

3. Components of the Horizontal Heat Advection

This study mainly considers three advection components: the elevation advection, the shear advection, and the Ekman advection. The spatial and temporal variations of the advection components are represented in Figure 2. The total advection shows an almost identical pattern with the elevation advection (Figures 2a and 2b), which is approximately one-order stronger than the shear advection and the Ekman advection (Figures 2c and 2d). Strong positive elevation advection values on the order of $10^{-5}°$C/s are found at the southern end of MAB around Cape Hatteras, but turns to be negative in the Southern Atlantic Bight. The magnitude of the shear advection increases southward, while that of the Ekman advection decreases southward.

Concerning the domain-averaged temporal variation (Figure 2e), the mean values of elevation, shear, and Ekman advections are 3.1 ($\pm$4.5) $\times$ $10^{-7}°$C/s, -0.78 ($\pm$0.37) $\times$ $10^{-7}°$C/s, and 0.47 ($\pm$1.0) $\times$ $10^{-7}°$C/s, respectively (values in the bracket indicate the standard deviation). The elevation advection, which is driven by the sea level pressure, is the dominant component. The signs of the elevation and Ekman advection are mostly positive, resulting in a positive total surface advection which causes the shelf to lose heat. This is not surprising by recalling that the mean flow on the continental shelf is equatorward from northeast to southwest approximately along the isobaths [*Fairbanks*, 1982; *Chapman et al.*, 1986; *Lentz*, 2008], The horizontal transport brings colder upstream water southward, causing the decrease of the heat content on the shelf.
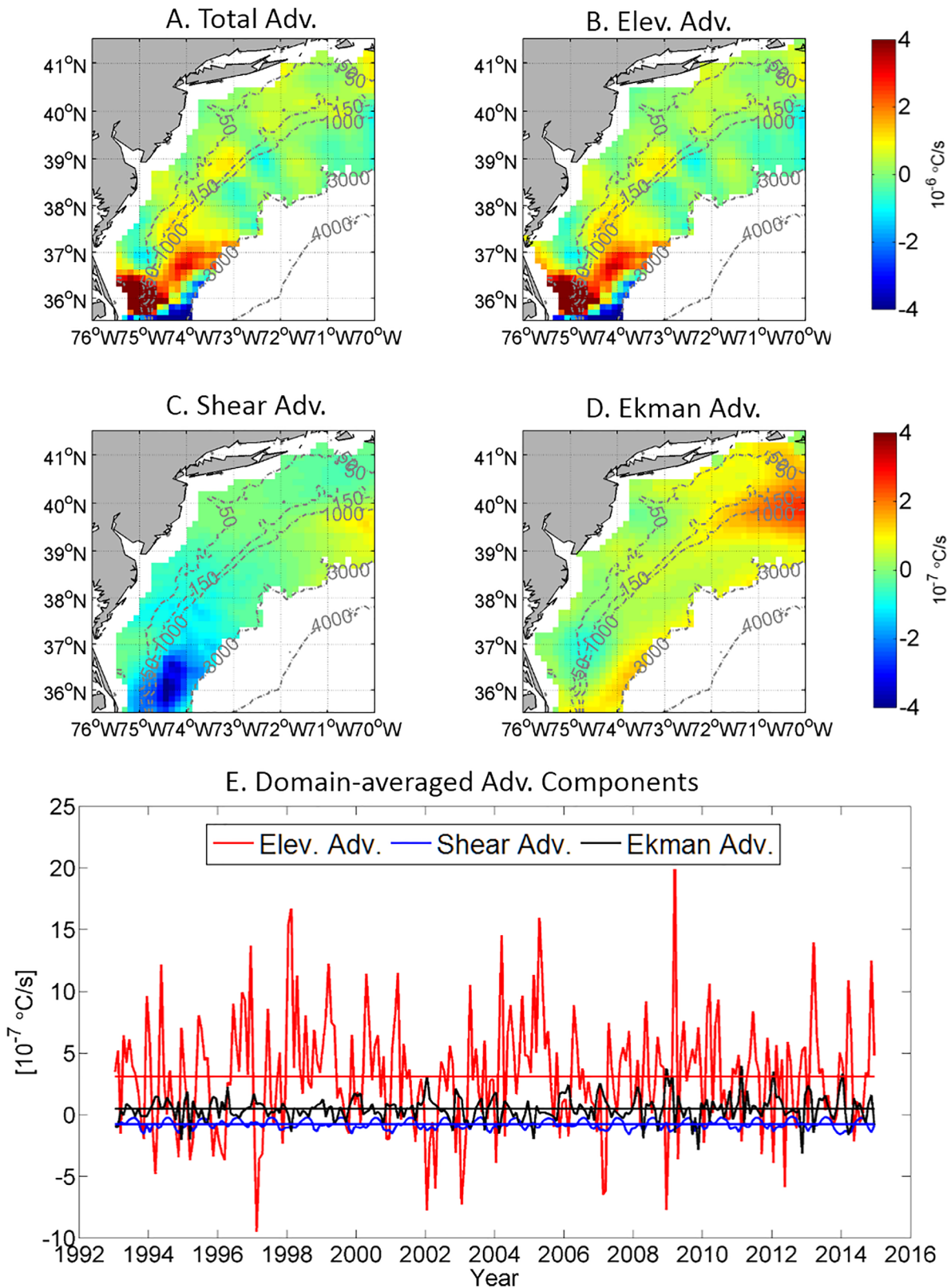
As revealed in Figure 2, the elevation advection is stronger than the Ekman advection within the mixed layer depth over the shelf, especially for the southern part of the shelf. Our results here do not conflict with previous studies which recognized the wind forcing as one of the important factors to the offshore transport within the New Jersey shelf [*Kohut et al.*, 2004; *Glenn et al.*, 2007; *Jiang*, 2008; *Dzwonkowski et al.*, 2009]. In the conventional Ekman theory, the magnitude of the wind-induced flow decreases as depth increases, implying the Ekman heat advection at the surface is stronger than the depth-averaged one within the mixed layer. Thus if we only consider the heat advection at the sea surface (which means the thermal wind shear can be neglected and the seasonal oscillation of the mixed layer depth is excluded), and follow the analytical Ekman model to estimate the wind-induced current at the surface instead of using the depth-averaged velocities, the wind-induced heat advection then increases to the same order to the geostrophic advection especially during winter times (Figure 3).

The advections are further decomposed in the alongshore and offshore components (Figure 4) corresponding to the alongshore and offshore currents. The alongshore (offshore) direction is defined based on the bathymetry gradient with positive sign pointing to approximately the northeast (southwest). For the elevation advection (Figures 4a and 4b), the offshore component is relatively strong in the shelf break region especially in the southern part of the MAB. The alongshore elevation advection is high at the northern and the southern end of MAB and low in the middle MAB, with positive advection on the shelf but stronger and negative advection along the shelf break. For the shear advection (Figures 4c and 4d), stronger negative values in the southern part indicate that the shear advection goes against the elevation advection and tend to warm up shelf water. For the Ekman advection (Figures 4e and 4f), coherent patterns are found all over the shelf except in the southern end of MAB, and the offshore component dominants.

The observed spatial viabilities of advection components are determined by the distributions of both the temperature gradient and the circulations over the shelf, which may further relate to various ocean dynamic processes subjected to regional differences. One example is the existence of the warm slope water and the Gulf Stream (and thus the increased temperature gradient) [*Lentz*, 2009] in the southern MAB, which may partially explain the southward intensification of the heat advection all through these advection components. Also, the occurring of the shelf break fronts [*Linder and Gawarkiewicz*, 1998; *Flagg et al.*, 2006] are probably related to the stronger heat advection along the shelf break region (Figure 4a). The linkage between patterns revealed here and oceanic processes is worth of further detailed investigation in the future.

We also investigated the domain-averaged temperature gradient and the barotropic geostrophic current separately (Figure 5). The temperature gradient is stronger in the offshore direction, while the geostrophic current is stronger in the alongshore direction. As a result, the heat advection component in the offshore direction is stronger than the alongshore one but are still of the same order.

Figure 2. The surface layer heat advection on the shelf. (a) The total advection. (b) The elevation advection. (c) The shear advection. (d) The Ekman advection. (e) Domain-averaged advection components from 1993 to 2014. The red line is the elevation advection. The blue line is the shear Advection. The solid black line is the Ekman advection. The horizontal lines indicate the temporal means. The unit of Figures 2a and 2b is one-order larger than that of Figures 2c and 2d.
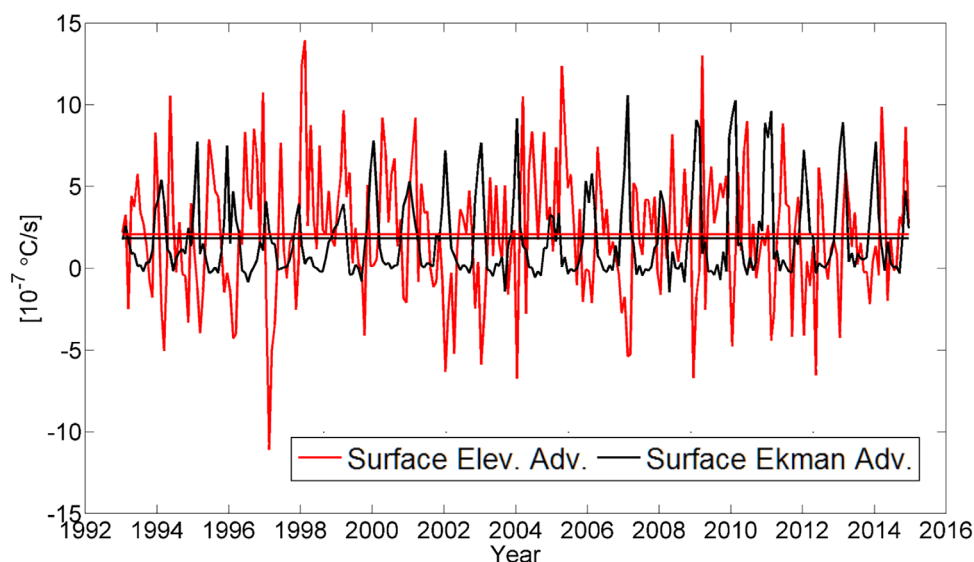
Figure 3. The domain-averaged heat advection comparison only at the surface between the elevation advection and the Ekman advection.

Moreover, a cross-shelf diagnostic along a transect off the New Jersey (Figure 6) also demonstrates that over the middle shelf the alongshore barotropic geostrophic advection is the dominant component, and over the shelf break region the offshore geostrophic advection is even stronger, while the shear advections and Ekman advections are relatively small.

4. Temporal Decomposition of the Horizontal Heat Advection

As revealed in Figure 2e, the advection components have strong temporal variations. One question then rises naturally as what determines the temporal variation of the heat advection. In this section, we take the elevation advection, the dominant heat advection over the shelf, as the study case. Similar analysis could also be done for the shear advection and Ekman advection but will not be discussed here. Still, SST is assumed to represent the MLT. The geostrophic currents from MADT are the depth-independent component of the geostrophic currents.

As described in section 2.5, both the temperature and the current can be decomposed using FMEEDM as an ensemble of five modes on different time scales (subseasonal, seasonal, interannual, long-term modes, and the mean). Thus the corresponding heat advection (equation (4)) has 25 modes and is summarized as the 5×5 matrix in Table 1. The advection component from the mean temperature by the mean current is constant of 3.0×10^{-7}°C/s. The standard deviation (STD) of other components ranges from 4.3×10^{-8}°C/s to 1.6×10^{-6}°C/s. The contribution factor as in section 2.5 is introduced to describe the relative magnitudes of these STDs. The largest three components are the products associated with the seasonal temperature by the mean current, the mean temperature by the subseasonal current, and the seasonal temperature by the subseasonal current, which account for 80% of the total energy.

We also noted that advection components resulted from the temporal mean, either the mean of the temperature or the current, totally accounted for 46.5% of the variation. In another words, the "background" temperature and current are playing important roles in the advection variation. The energy contribution revealed in Table 1 is consistent with the spectral distribution of the SST and surface geostrophic currents (Figures 7a and 7b). The spectrum of the temperature peaks at the 1 cpy driven by the seasonal oscillation of the surface heat flux, while multipeaks are found within the subseasonal portion of the surface geostrophic currents.

Furthermore, the results suggest that the energy of the advection is transferred through different time scales due to the cross-spectral interaction, One example is the advection of the seasonal temperature by the seasonal current. The corresponding advection term in the frequency domain contains a peak at 2 cpy
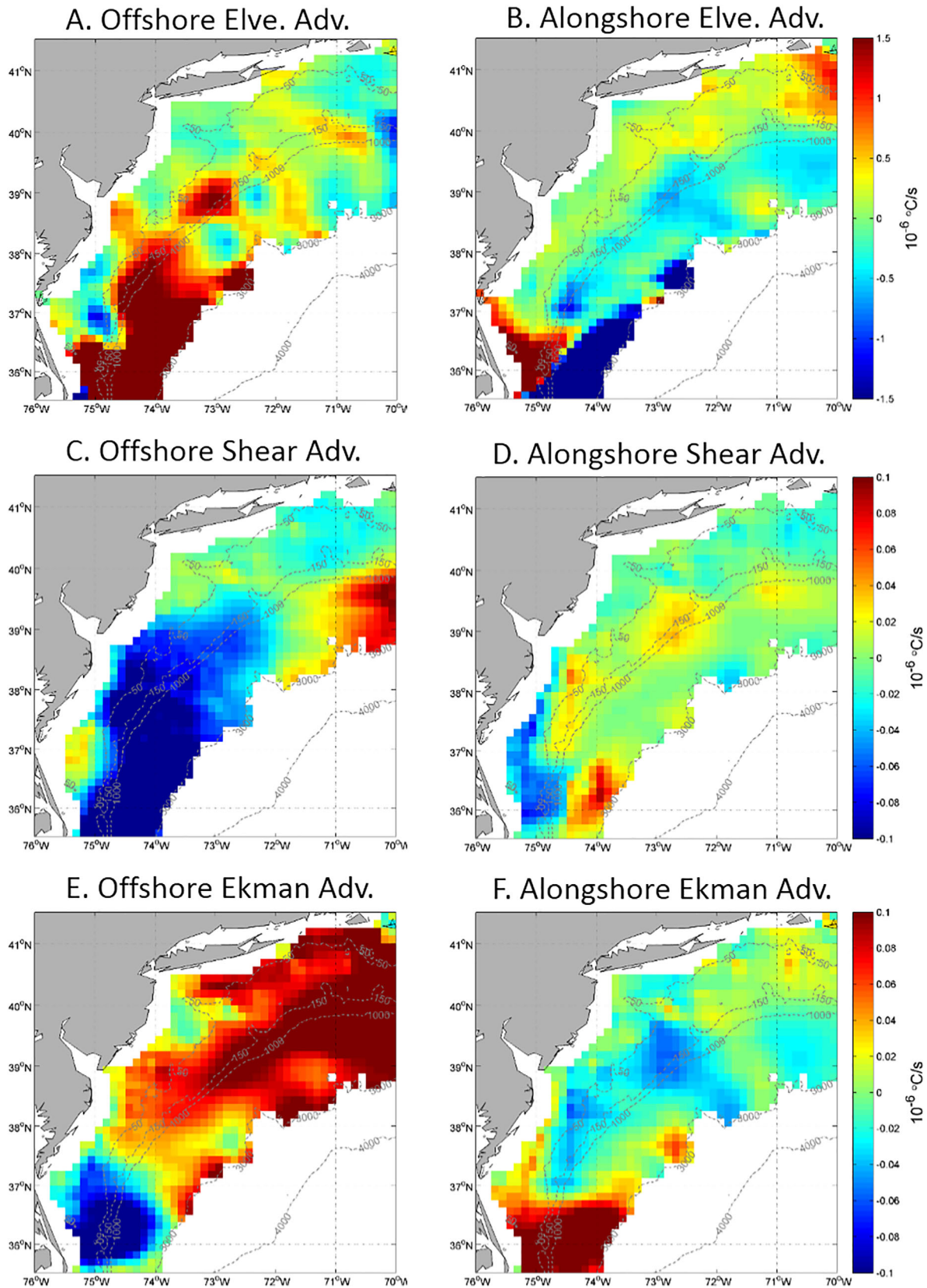
Figure 4. The temporal mean of the alongshore and offshore advection components. (top: a, b) The elevation advection. (middle: c, d) The shear advection. (bottom: e, f) The Ekman advection. The left column figures (a, c, e) are in offshore direction. The right column figures (b, d, f) are in the alongshore direction.
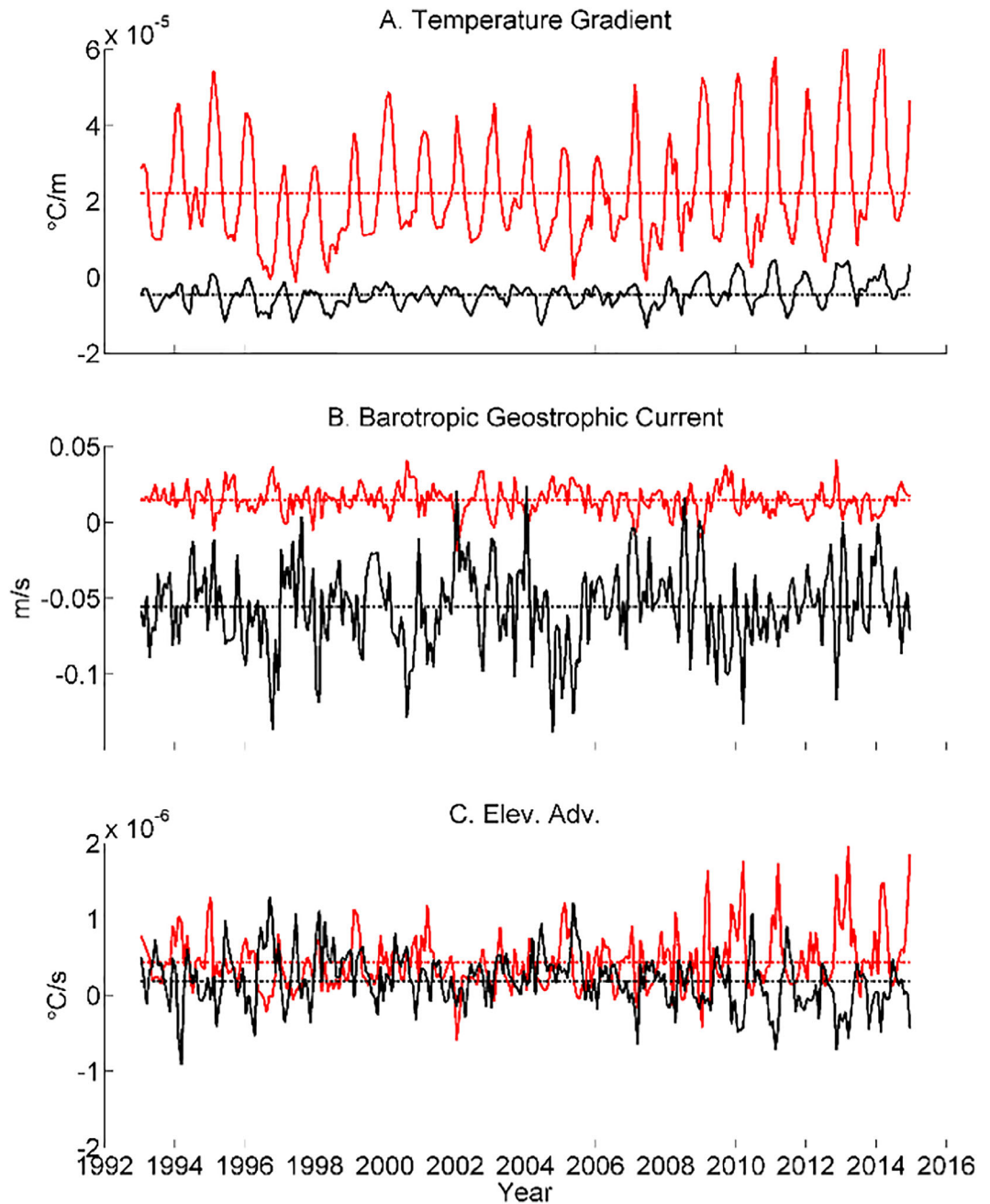
Figure 5. Domain-averaged comparison between the alongshore and offshore barotropic geostrophic heat advection. (a) Temperature gradient. (b). Barotropic geostrophic current. (c) The corresponding heat advection. Black lines are in the alongshore direction while red lines are in the offshore direction. Dashed lines are the temporal means.

(semiannual scale) and a trough at 1 cpy (seasonal scale). The energy flows from the annual scale to the semiannual scale. The semiannual signal (Figure 7e) is of the same order $(10^{-12}(^{\circ}C/s)^2/cpy)$ as is contained within the total advection (Figure 7d), and is even the same order as the semiannual oscillation contained in the heat storage (Figure 7c). In this process, the energy within the seasonal oscillation is flowing into the semiannual time scale, as well as lower frequency domain (which is straight forward from trigonometry). Meanwhile, the total advection still peaks at 1 cpy, suggesting the energy of the annual scale is also being replenished. Possibly there are two replenishing pathways: first, from the retaining of the original seasonal oscillations (e.g., the advection of the seasonal temperature by the mean current). Second, from the newly generated seasonal bands in the cross-spectral interaction. As a result of the cross-spectral interactions
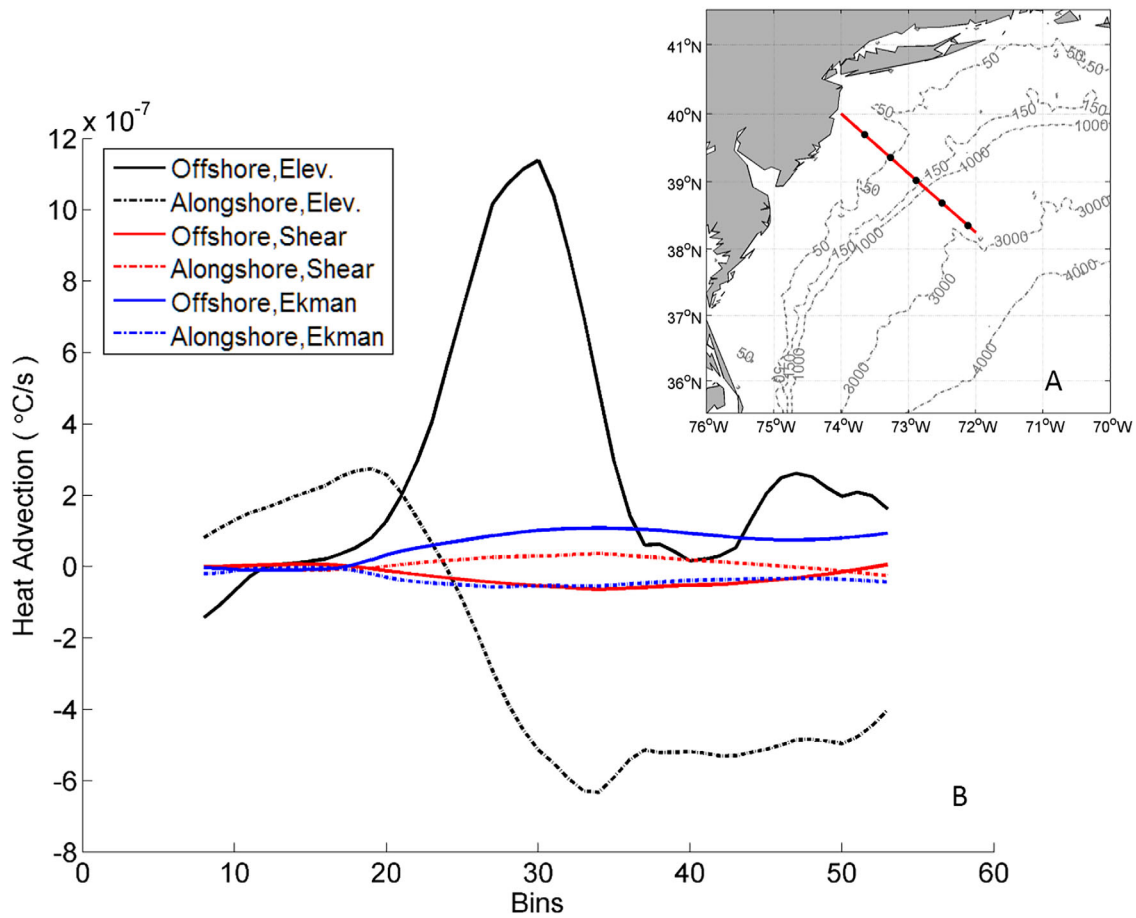
Figure 6. Diagnostic analysis along a cross-shelf transect. (a) The location of the transect. The black dots indicate the location of the 10th, 20th, 30th, 40th, and 50th bins along the transect. (b) The advection components along the transect, starting from the inner shelf, ending in the open ocean. The shelf break region is around the 30th bin.

between the temperature and the current, the energy is redistributed in the heat advection, generating the nonlinear temporal variation.

5. Discussion

Concerning the heat advection driven by the barotropic geostrophic current, the alongshore component is smaller than the offshore one due to the strong current but weak temperature gradient in the alongshore direction. However, it should be noted that most of the strong advection values are focused on the southern end of MAB around Cape Hatteras. This area is known with the shelf water veering offshore and being entrained with the Gulf Stream, as well as the slope water and Gulf Stream intrusion [e.g., *Bane et al.*, 1988;

Table 1. The Temporal Decomposition of the Horizontal Heat Advection Associated With the Surface Geostrophic Current[a]

		Surface Geostrophic Current					
		Subseasonal	Seasonal	Interannual	Long-Term	Mean	Row Sum
SST	Subseasonal	**1.3%**	0.2%	0.2%	0.1%	**1.5%**	3.2%
	Seasonal	**39.4%**	3.6%	**5.0%**	1.4%	**23.0%**	**72.4%**
	Interannual	**0.8%**	0.1%	0.1%	0.0%	**0.7%**	1.8%
	Long-Term	**1.0%**	0.1%	0.1%	0.0%	**1.0%**	2.3%
	Mean	**16.1%**	1.8%	1.9%	0.6%		**20.3%**
	Column Sum	**58.6%**	5.7%	7.3%	2.2%	**26.2%**	

[a]The percentages present the contribution of each component to the total energy (derived from the contribution factor). The major components are highlighted in bold.
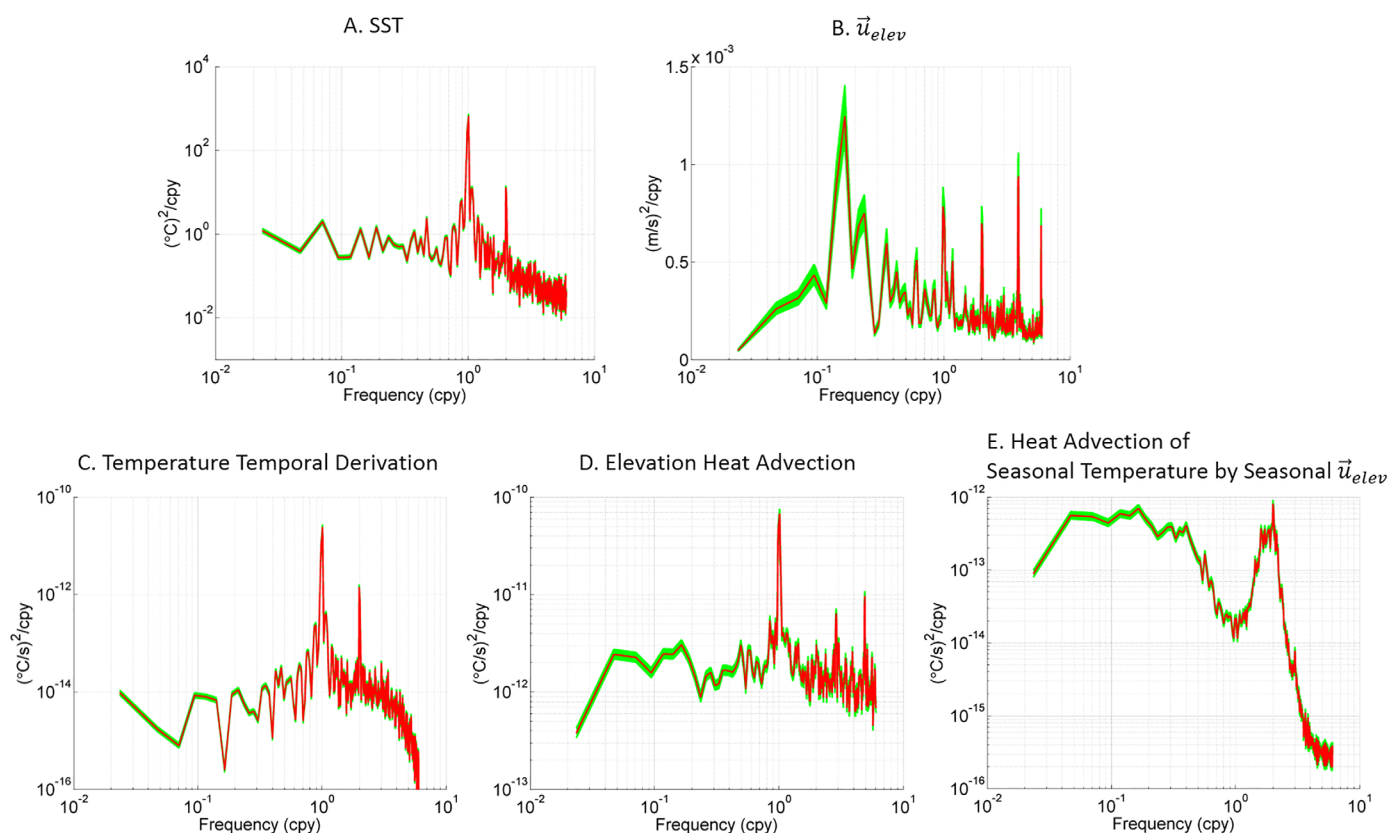
Figure 7. Domain-averaged power spectral densities of: (a) SST, (b) surface barotropic geostrophic current $\vec{u}_{elev}$, (c) temporal derivation of temperature, (d) the horizontal heat advection due to $\vec{u}_{elev}$, and (e) the heat advection component of the seasonal temperature by the seasonal $\vec{u}_{elev}$. Green areas represent the 95% confidence interval for the spectrum [*Thomson and Emery*, 2014]. Red lines are domain-averaged values.

Churchill and Berger, 1998]. *Churchill and Gawarkiewicz* [2012] also suggests the approaching of the Gulf Stream to the shelf may enhance the offshore transport. With the southern end of MAB (south of 37°N) excluded from the averaging domain, however, the barotropic geostrophic heat advection still dominant the horizontal heat advection, while the domain-averaged offshore barotropic advection reduces to almost the same magnitude as the alongshore advection especially along the shelf break region (see also Figure 6). Including the southern MAB or not, the heat exchange between the shelf and the ambient ocean is as important as the alongshore heat advection over the shelf. *Lentz* [2010] found that if using the surface heat flux from OAFlux, the cross-shelf heat flux is required to balance the alongshore heat flux, while using surface heat flux from other data sets (NCEP) indicates the offshore heat flux is small. In this study, our results from direct advective heat flux estimation also imply that the cross-shelf heat flux could not be neglected.

The components on different time scale within the heat advection are quantitatively assessed (Table 1). New frequency components are generated in the heat advection as a result of the cross-spectral interactions between the temperature and the currents, and the energy within certain time scales is redistributed. Due to the nonlinear nature of the interaction process, it would be difficult to quantify the detailed amount of energy being transferred or retained. However, recalling from section 4, those advection components involved with the mean component of either the temperature or the current account for about 46.5% of the total variation without any new frequency generated. This at least provides a baseline of the energy retained within the original band. The cross-spectral effect revealed here also suggests that the possibility that the temperature oscillations on seasonal time scales can partially affect interannual variability of the heat flux, and long-term temperature trend may contribute to the short-term extreme events. One similar example is the Indian Summer Monsoon, whose interannual variability is revealed to be influenced by the seasonal mean and the intraseasonal oscillation concerning the kinetic energy [*Suhas et al.*, 2012]. These cross-spectral interactions within the heat advection are necessarily subject to further investigation to fully clarify the response of the ocean heat content to variations on different time scales.

6. Summary

In this study, multisensor satellite data are used to investigate the spatial and temporal properties of the surface horizontal heat advection over the MAB. Three major current components, driven by the sea level pressure, the density gradient, and the wind-induced Ekman transport, respectively, are considered in this study. Corresponding advection components (the elevation advection, shear advection, and Ekman advection) are compared over the shelf and their spatial distributions are described. The total heat advection over the shelf is mostly positive, suggesting that the role of the heat advection is cooling the shelf by bringing cold water southward.

We found that the domain-averaged elevation advection is one-order larger than the shear advection and the Ekman advection. As a result, the total heat advection shows an almost identical spatial pattern with the elevation advection. These advections are further decomposed in the alongshore and offshore direction. Diagnostics along a transect off the New Jersey shelf revealed that the alongshore elevation advection is the largest one over the middle shelf, while for the shelf break region the offshore elevation advection is of the same order as the alongshore one. This implies both the alongshore and offshore heat flux are important over the shelf.

We choose the dominant heat advection, the elevation advection, to be analyzed in the frequency domain to further investigate the temporal properties of the heat advection. Both the temperature and the current are decomposed using FMEEMD into five components (subseasonal, seasonal, interannual, long-term modes, and the mean) thus there are a 5×5 matrix of the advection components. The magnitude distribution of these advections is determined by the spectrum of the temperature and currents. Taking the advection from the seasonal temperature and the seasonal current, we found that the energy within the advection is redistributed through different time scales. And those advections involving with the mean component, either the mean of the temperature or the current, account for 46.5% of the total advection variations and actually indicate the energy retained within the original band. Our results here provide a baseline for the further understanding of the nonlinear energy transfer framework between different time scales in the heat advection, and implies the possibility of the mutual influence of ocean phenomena on different time scales.

Appendix A: The Comparison Between Different MLD

In the heat budget estimation, the integration depth is chosen as the MLD determined from the 12 month gridded climatological thermal field from WOA, which implies that the MLD interannual variability is omitted. To estimate the uncertainty induced, we introduce the temperature profiles simulated in the SODA data as a preliminary comparison.
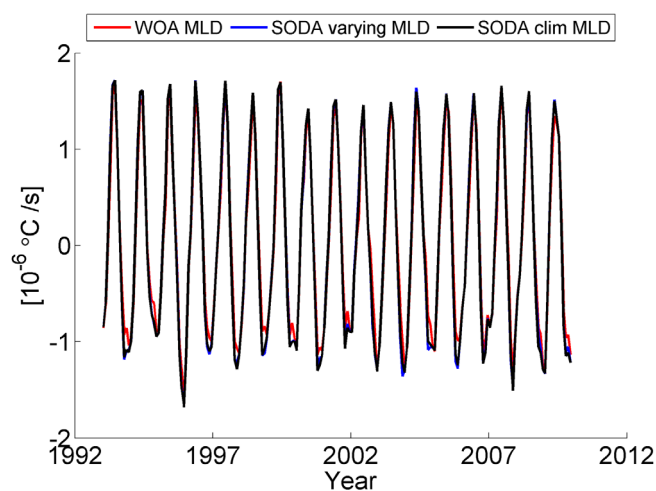
Figure A1. Cross-comparison of the temporal heat variation with different choice of MLD. The mixed layers are WOA MLD, SODA time-varying MLD, and SODA monthly climatological MLD, respectively. This is the vertical mean thus the unit is °C/s.

Totally there are three MLDs compared here: (1) the 12 month MLD determined from the thermal field of WOA; (2) the monthly MLD (thus varying year by year) determined from thermal field of SODA; and (3) The 12 month climatological MLD determined from SODA. The mixed layer temperatures are also from SODA thus varies vertically. As shown in Figure A1, all curves are showing similar seasonal variability. Using time varying MLD and climatological MLD from SODA are almost identical, whose amplitude are slightly larger than using WOA MLD in the winter. The root mean squared error (RMSE) is 1.7×10^{-7}°C/s between the advection using WOA MLD and SODA varying MLD, and is 5.6×10^{-8}°C/s between SODA climatological MLD and SODA varying MLD.

References

Bane, J. M., O. B. Brown, R. H. Evans, and P. Hamilton (1988), Gulf Stream remote forcing of shelfbreak currents in the Mid-Atlantic Bight, *Geophys. Res. Lett.*, *15*(5), 405–407, doi:10.1029/GL015i005p00405.

Beardsley, R. C., S. J. Lentz, R. A. Weller, R. Limeburner, J. D. Irish, and J. B. Edson (2003), Surface forcing on the southern flank of Georges Bank, February–August 1995, *J. Geophys. Res.*, *108*(C11), 8007, doi:10.1029/2002JC001359.

Carton, J. A., B. S. Giese, and S. A. Grodsky (2005), Sea level rise and the warming of the oceans in the Simple Ocean Data Assimilation (SODA) ocean reanalysis, *J. Geophys. Res.*, *110*, C09006, doi:10.1029/2004JC002817.

Chapman, D. C., J. A. Barth, R. C. Beardsley, and R. G. Fairbanks (1986), On the Continuity of Mean Flow between the Scotian Shelf and the Middle Atlantic Bight, *J. Phys. Oceanogr.*, *16*(4), 758–772, doi:10.1175/1520-0485(1986)016<0758:OTCOMF>2.0.CO;2.

Chen, X., and K.-K. Tung (2014), Varying planetary heat sink led to global-warming slowdown and acceleration, *Science*, *345*(6199), 897–903, doi:10.1126/science.1254937.

Cheney (1994), TOPEX/POSEIDON: The 2-cm solution: Cheney – 2012, *J. Geophys. Res.*, *99*(C12), 24,555–24,563.

Churchill, J. H., and T. J. Berger (1998), Transport of Middle Atlantic Bight shelf water to the Gulf stream near cape Hatteras, *J. Geophys. Res. Oceans*, *103*(C13), 30,605–30,621, doi:10.1029/98JC01628.

Churchill, J. H., and G. G. Gawarkiewicz (2012), Pathways of shelf water export from the Hatteras shelf and slope, *J. Geophys. Res. Oceans*, *117*, C08023, doi:10.1029/2012JC007995.

Connolly, T. P., and S. J. Lentz (2014), Interannual variability of wintertime temperature on the inner continental shelf of the Middle Atlantic Bight, *J. Geophys. Res. Oceans*, *119*, 6269–6285, doi:10.1002/2014JC010153.

Cushman-Roisin, B., and J.-M. Beckers (2011), *Introduction to Geophysical Fluid Dynamics: Physical and Numerical Aspects*, Elsevier, vol. 101, Academic Press, Cambridge, U. K.

de Boyer Montégut, C., J. Mignot, A. Lazar, and S. Cravatte (2007), Control of salinity on the mixed layer depth in the world ocean: 1. General description, *J. Geophys. Res.*, *112*, C06011, doi:10.1029/2006JC003953.

Dong, S., and K. A. Kelly (2004), Heat budget in the Gulf Stream region: The importance of heat storage and advection, *J. Phys. Oceanogr.*, *34*(5), 1214–1231, doi:10.1175/1520-0485(2004)034<1214:HBITGS>2.0.CO;2.

Dzwonkowski, B., J. T. Kohut, and X.-H. Yan (2009), Seasonal differences in wind-driven across-shelf forcing and response relationships in the shelf surface layer of the central Mid-Atlantic Bight, *J. Geophys. Res.*, *114*, C08018, doi:10.1029/2008JC004888.

Fairbanks, R. G. (1982), The origin of continental shelf and slope water in the New York Bight and Gulf of Maine: Evidence from H218O/H216O ratio measurements, *J. Geophys. Res.*, *87*(C8), 5796–5808, doi:10.1029/JC087iC08p05796.

Feng, J., Z. Wu, and G. Liu (2014), Fast Multidimensional Ensemble Empirical Mode Decomposition Using a Data Compression Technique, *J. Clim.*, *27*(10), 3492–3504, doi:10.1175/JCLI-D-13-00746.1.

Flagg, C. N., M. Dunn, D.-P. Wang, H. T. Rossby, and R. L. Benway (2006), A study of the currents of the outer shelf and upper slope from a decade of shipboard ADCP observations in the Middle Atlantic Bight, *J. Geophys. Res.*, *111*, C06003, doi:10.1029/2005JC003116.

Garratt, J. R. (1994), *The Atmospheric Boundary Layer*, Cambridge Univ. Press, Cambridge, U. K.

Gawarkiewicz, G. G., R. E. Todd, A. J. Plueddemann, M. Andres, and J. P. Manning (2012), Direct interaction between the Gulf Stream and the shelfbreak south of New England, *Sci. Rep.*, *2*, 553, doi:10.1038/srep00553.

Glenn, S., O. Schofield, R. Chant, J. Kohut, H. Roarty, J. Bosch, L. Bowers, D. Gong, and J. Kerfoot (2007), Wind-driven response of the Hudson River Plume and its effect on dissolved oxygen concentrations, *Environ. Res. Eng. Manage.*, *1*, 14–18.

Grodsky, S. A., J. A. Carton, and H. Liu (2008), Comparison of bulk sea surface and mixed layer temperatures, *J. Geophys. Res.*, *113*, C10026, doi:10.1029/2008JC004871.

Grodsky, S. A., N. Reul, B. Chapron, J. A. Carton, and F. O. Bryan (2017), Interannual surface salinity on Northwest Atlantic shelf, *J. Geophys. Res. Oceans*, *122*, doi:10.1002/2016JC012580.

Gulev, S. K., M. Latif, N. Keenlyside, W. Park, and K. P. Koltermann (2013), North Atlantic Ocean control on surface heat flux on multidecadal timescales, *Nature*, *499*(7459), 464–467, doi:10.1038/nature12268.

Halliwell, G. R. (1998), Simulation of North Atlantic Decadal/Multidecadal Winter SST Anomalies Driven by Basin-Scale Atmospheric Circulation Anomalies, *J. Phys. Oceanogr.*, *28*(1), 5–21, doi:10.1175/1520-0485(1998)028<0005:SONADM>2.0.CO;2.

Han, G., K. Ohashi, N. Chen, P. G. Myers, N. Nunes, and J. Fischer (2010), Decline and partial rebound of the Labrador Current 1993–2004: Monitoring ocean currents from altimetric and conductivity-temperature-depth data, *J. Geophys. Res.*, *115*, C12012, doi:10.1029/2009JC006091.

He, R., and R. H. Weisberg (2002), West Florida shelf circulation and temperature budget for the 1999 spring transition, *Cont. Shelf Res.*, *22*(5), 719–748, doi:10.1016/S0278-4343(01)00085-1.

He, R., and R. H. Weisberg (2003), West Florida shelf circulation and temperature budget for the 1998 fall transition, *Cont. Shelf Res.*, *23*(8), 777–800, doi:10.1016/S0278-4343(03)00028-1.

Huang, N. E., Z. Shen, S. R. Long, M. C. Wu, H. H. Shih, Q. Zheng, N.-C. Yen, C. C. Tung, and H. H. Liu (1998), The empirical mode decomposition and the Hilbert spectrum for nonlinear and non-stationary time series analysis, *Proc. R. Soc. London Ser. A*, *454*(1971), 903–995, doi:10.1098/rspa.1998.0193.

Jiang, L. (2008), A comprehensive study on coastal upwelling using observations, models and proxies, University of Delaware, Newark, DE.

Kohut, J. T., S. M. Glenn, and R. J. Chant (2004), Seasonal current variability on the New Jersey inner shelf, *J. Geophys. Res.*, *109*, C07S07, doi:10.1029/2003JC001963.

Kushnir, Y. (1994), Interdecadal variations in North Atlantic sea surface temperature and associated atmospheric conditions, *J. Clim.*, *7*(1), 141–157, doi:10.1175/1520-0442(1994)007<0141:IVINAS>2.0.CO;2.

Lee, Y. J., and K. Lwiza (2005), Interannual variability of temperature and salinity in shallow water: Long Island Sound, New York, *J. Geophys. Res. Oceans*, *110*, C09022, doi:10.1029/2004JC002507.

Lentz, S. J. (1992), The surface boundary layer in coastal upwelling regions, *J. Phys. Oceanogr.*, *22*, 1517–1539, doi:10.1175/1520-0485.

Lentz, S. J. (2008), Observations and a model of the mean circulation over the Middle Atlantic Bight continental shelf, *J. Phys. Oceanogr.*, *38*(6), 1203–1221, doi:10.1175/2007JPO3768.1.

Lentz, S. J. (2009), The mean along-isobath heat and salt balances over the Middle Atlantic Bight continental shelf, *J. Phys. Oceanogr.*, *40*(5), 934–948, doi:10.1175/2009JPO4214.1.

Lentz, S. J., R. K. Shearman, and A. J. Plueddemann (2010), Heat and salt balances over the New England continental shelf, August 1996 to June 1997, *J. Geophys. Res.*, *115*, C07017, doi:10.1029/2009JC006073.

Levitus, S. et al. (2012), World ocean heat content and thermosteric sea level change (0–2000 m), 1955–2010, *Geophys. Res. Lett.*, *39*, L10603, doi:10.1029/2012GL051106.

Linder, C. A., and G. Gawarkiewicz (1998), A climatology of the shelfbreak front in the Middle Atlantic Bight, *J. Geophys. Res.*, *103*(C9), 18,405–18,423, doi:10.1029/98JC01438.

Locarnini, R. A. et al. (2013), *World Ocean Atlas 2013, Volume 1: Temperature*, edited by S. Levitus, and A. Mishonov, NOAA Atlas NESDIS, *73*, 40 pp., Silver Spring, Md.

Mountain, D. G., G. A. Strout, and R. C. Beardsley (1996), Surface heat flux in the Gulf of Maine, *Deep Sea Res., Part II*, *43*(7–8), 1533–1546, doi:10.1016/S0967-0645(96)00057-4.

Peng, G., H.-M. Zhang, H. P. Frank, J.-R. Bidlot, M. Higaki, S. Stevens, and W. R. Hankins (2013), Evaluation of various surface wind products with OceanSITES buoy measurements, *Weather Forecast.*, *28*(6), 1281–1303, doi:10.1175/WAF-D-12-00086.1.

Ponte, R. M. (1994), Understanding the relation between wind- and pressure-driven sea level variability, *J. Geophys. Res.*, *99*(C4), 8033–8039, doi:10.1029/94JC00217.

Reynolds, R. W., T. M. Smith, C. Liu, D. B. Chelton, K. S. Casey, and M. G. Schlax (2007), Daily High-Resolution-Blended Analyses for Sea Surface Temperature, *J. Clim.*, *20*(22), 5473–5496, doi:10.1175/2007JCLI1824.1.

Rio, M. H., S. Guinehut, and G. Larnicol (2011), New CNES-CLS09 global mean dynamic topography computed from the combination of GRACE data, altimetry, and in situ measurements, *J. Geophys. Res.*, *116*, C07018, doi:10.1029/2010JC006505.

Ruiz Etcheverry, L. A., M. Saraceno, A. R. Piola, and P. T. Strub (2016), Sea level anomaly on the Patagonian continental shelf: Trends, annual patterns and geostrophic flows, *J. Geophys. Res. Oceans*, *121*, 2733–2754, doi:10.1002/2015JC011265.

Ruiz, S., A. Pascual, B. Garau, Y. Faugère, A. Alvarez, and J. Tintoré (2009), Mesoscale dynamics of the Balearic Front, integrating glider, ship and satellite data, *J. Mar. Syst.*, *78*, supplement, S3–S16, doi:10.1016/j.jmarsys.2009.01.007.

Sha, J., Y.-H. Jo, X.-H. Yan, and W. T. Liu (2015), The modulation of the seasonal cross-shelf sea level variation by the cold pool in the Middle Atlantic Bight, *J. Geophys. Res. Oceans*, *120*, 7182–7194, doi:10.1002/2015JC011255.

Shearman, R. K., and S. J. Lentz (2009), Long-term sea surface temperature variability along the U.S. East coast, *J. Phys. Oceanogr.*, *40*(5), 1004–1017, doi:10.1175/2009JPO4300.1.

Strub, P. T., C. James, V. Combes, R. Matano, A. Piola, E. Palma, M. Saraceno, R. Guerrero, H. Fenco, and L. Ruiz Etcheverry (2015), Altimeter-derived seasonal circulation on the Southwest Atlantic shelf: 27°–43°S, *J. Geophys. Res. Oceans*, *120*, 3391–3418, doi:10.1002/2015JC010769.

Suhas, E., J. M. Neena, and B. N. Goswami (2012), Interannual variability of Indian summer monsoon arising from interactions between seasonal mean and intraseasonal oscillations, *J. Atmos. Sci.*, *69*(6), 1761–1774, doi:10.1175/JAS-D-11-0211.1.

Thomson, R. E., and W. J. Emery (2014), *Data Analysis Methods in Physical Oceanography*, 3rd ed., Elsevier, Amsterdam.

Wu, Z., and N. E. Huang (2009), Ensemble empirical mode decomposition: A noise-assisted data analysis method, *Adv. Adapt. Data Anal.*, *1*(1), 1–41, doi:10.1142/S1793536909000047.

Wu, Z., N. E. Huang, and X. Chen (2009), The multi-dimensional ensemble empirical mode decomposition method, *Adv. Adapt. Data Anal.*, *1*(3), 339–372, doi:10.1142/S1793536909000187.

Yeh, J.-R., J.-S. Shieh, and N. E. Huang (2010), Complementary ensemble empirical mode decomposition: A novel noise enhanced data analysis method, *Adv. Adapt. Data Anal.*, *2*(2), 135–156, doi:10.1142/S1793536910000422.

Zhang, H.-M., J. J. Bates, and R. W. Reynolds (2006), Assessment of composite global sampling: Sea surface wind speed, *Geophys. Res. Lett.*, *33*, L17714, doi:10.1029/2006GL027086.